

Highlights

- Neural trajectories in the hippocampus exhibited greater variability during a working memory (WM) task compared to those in the entorhinal cortex and amygdala regions.
- The distance of neural trajectories between encoding and retrieval states in the hippocampus was memory-load dependent during a WM task.
- Hippocampal neural trajectories fluctuated between the encoding and retrieval states in a task-dependent manner during both baseline and sharp-wave ripple (SWR) periods.
- Hippocampal neural trajectories shifted from encoding to retrieval states during SWR period.

Hippocampal neural fluctuations between memory encoding and retrieval states during a working memory task in humans: Encoding-to-retrieval shift during sharp-wave ripples

Yusuke Watanabe^{a,*}, Yuji Ikegaya^{b,c,d}, Takufumi Yanagisawa^{a,e}

^a*Institute for Advanced Cocreation studies, Osaka University, 2-2 Yamadaoka, Suita, 565-0871, Osaka, Japan*

^b*Graduate School of Pharmaceutical Sciences, The University of Tokyo, 7-3-1 Hongo, Tokyo, 113-0033, Japan*

^c*Institute for AI and Beyond, The University of Tokyo, 7-3-1 Hongo, Tokyo, 113-0033, Japan*

^d*Center for Information and Neural Networks, National Institute of Information and Communications Technology, 1-4 Yamadaoka, Suita City, 565-0871, Osaka, Japan*

^e*Department of Neurosurgery, Osaka University Graduate School of Medicine, 2-2 Yamadaoka, Osaka, 565-0871, Japan*

Abstract

Working memory (WM) is crucial for a multitude of cognitive functions, yet the intricacies of the neural mechanisms at play remain to be fully comprehended. Interestingly, the hippocampus and sharp-wave ripple complexes (SWRs) — succinct, synchronous neural events in the hippocampus — garner recognition for their significance in memory consolidation and retrieval, albeit their correlation with WM tasks is yet to be clarified. Our current study suggests that multiunit activity patterns in the hippocampus may work in tandem with SWRs, thereby displaying unique dynamics during WM tasks. We examined a dataset comprising intracranial electroencephalogram recordings obtained from the medial temporal lobe (MTL) of nine epilepsy patients engaged in an eight-second Sternberg task. Gaussian-process factor analysis was employed to extract low-dimensional neural representations, termed 'trajectories', within the MTL regions during the WM task. Our findings indicate that the hippocampus exhibits the most pronounced variation in neural trajectory in comparison with the entorhinal cortex and amygdala. Moreover, the dissimilarity in trajectories measured between encoding and retrieval phases was found to be contingent on memory load. Significantly, the hippocampal trajectories oscillate during the retrieval phase, demonstrating task-dependent shifts between encoding and retrieval states, both during baseline and SWR events. This fluctuation transitions from encoding to retrieval states concurrent with the occurrence of SWRs. These discoveries reassert the pivotal role of the hippocampus in WM tasks and propose a fresh hypothesis: the hippocampus transitions its functional state from encoding to retrieval in the midst of SWRs.

Keywords: working memory, WM, memory load, hippocampus, sharp-wave ripples, SWR, humans

1. Introduction

Working memory (WM) is crucial in everyday life; however, its neural mechanism has yet to be fully elucidated. Specifically, the role of the hippocampus, an essential brain region contributing to memory has been an ongoing topic [1] [2] [3] [4] [5] [6] [7] [8] [9]. Understanding the hippocampus' role in working memory is instrumental in deepening our knowledge of cognitive processes, ultimately aiding in developing cognitive

training strategies and interventions.

It is known that a transient and synchronous oscillation called sharp-wave ripple (SWR) [10] is associated with various cognitive functions, including memory replay [11] [12] [13] [14] [15], memory consolidation [16] [17] [18] [19], memory recall [20] [21] [22], and neural plasticity [23] [24]. Thus, SWR might be a fundamental representation of processing in the hippocampus and contribute to working memory performances. However, investigations into the effects of SWRs on working memory remain infrequent ([25] and limited to

*Corresponding author. Tel: +81-6-6879-3652

rodent models using navigation tasks, in which precise timings of memory acquisition and recall are not separated.

Moreover, it is getting discovered that hippocampal neurons exhibit low-dimensional representations during WM tasks. For instance, the firing patterns of place cells [26] [27] [28] [29] [30] in the hippocampus were embedded within a dynamic, nonlinear three-dimensional hyperbolic geometry in rodent [31]. Furthermore, grid cells in the entorhinal cortex (EC) — the primary gateway to the hippocampus [32] [33] [34] — exhibited toroidal topology during exploration [35]. However, again, these experiments are limited to spatial navigation tasks in rodents so that the temporal resolution of WM tasks is constrained. Moreover, whether these findings are generalized to humans and beyond navigation tasks, are not investigated yet.

Given these backgrounds, in this study, we investigated the hypothesis that hippocampal neurons exhibit distinct representations in low-dimensional spaces as ‘neural trajectory’ during WM tasks, with a specific focus on SWR periods. To test this hypothesis, we utilized a dataset of patients performing an eight-second Sternberg task with high temporal resolution (1 s for fixation, 2 s for encoding, 3 s for maintenance, and 2 s for retrieval) while their intracranial electroencephalography signals (iEEG) in the medial temporal lobe (MTL) were recorded [36]. To explore low-dimensional neural trajectories, we employed Gaussian-process factor analysis (GPFA) based on multiunit activities, a proven tool for the analysis of neural population dynamics [37].

2. Methods

2.1. Dataset

A publicly accessible dataset [36] was employed, in which nine patients with epilepsy performed a modified Sternberg task that consisted of the following four phases: fixation (1 s), encoding (2 s), maintenance (3 s), and retrieval (2 s) [36]. During the encoding phase, participants were presented sets of either four, six, or eight alphabetical letters, referred to as set size. Subsequently, they were tasked with ascertaining whether a probe letter presented in the retrieval phase had been displayed (the correct choice for Match IN task) or not (the correct choice for Mismatch OUT task). iEEG signals were recorded at a sampling rate of 32 kHz, within

the frequency range of 0.5–5,000 Hz, using depth electrodes implanted in the MTL regions: the left and right hippocampal head (AHL and AHR), hippocampal body (PHL and PHR), entorhinal cortex (ECL and ECR), and amygdala (AL and AR) (Figure 1A and Table 1). Subsequently, iEEG signals were resampled at a rate of 2 kHz. Correlations were found among the experimental variables such as set size and correct rate (Figure ??S1). The timings of multiunit spikes were estimated by a spike sorting algorithm [38] by the Combinato package (<https://github.com/jniediek/combinato>) (Figure 1C).

2.2. Calculation of neural trajectories using GPFA

To calculate the neural trajectories (also referred to as factors; Figure 1D) in the hippocampus, EC, and amygdala (Figure 1D), GPFA [37], was employed on multiunit activity data for each session. GPFA was applied using the elephant package (<https://elephant.readthedocs.io/en/latest/reference/gpfa.html>). The bin size was set as 50 ms, without overlaps. Each factor was z-normalized across each session. From the trajectories, Euclidean distance from the origin (O) was calculated (Figure 1E).

For every trajectory within a region, such as AHL, *geometric medians* (*i.e.*, g_F for fixation, g_E for encoding, g_M for maintenance, and g_R for retrieval phase) were determined by calculating the median coordinates of trajectory during the four phases (Figure 1D). The optimal dimensionality for GPFA was determined as three via the elbow method utilizing the log-likelihood values using a three-fold cross-validation approach (Figure 2B).

2.3. Defining SWR candidates from hippocampal regions

To identify potential SWR events within the hippocampus, we employed a detection method aligned with a consensus in this field [39]. Specifically, local field potential (LFP) signals from a region of interest (ROI), such as AHL, were re-referenced by subtracting an averaged signal from outside of the ROI (*e.g.*, AHR, PHL, PHR, ECL, ECR, AL, and AR) (see Figure 1A). The re-referenced LFP signals were applied to a ripple-band filter (80–140

Hz) to isolate SWR candidates (= SWR⁺ candidates) (see Figure 1B). SWR detection was conducted using a published tool (https://github.com/Eden-Kramer-Lab/ripple_detection) [40], with modifications such as an updated bandpass range of 80–140 Hz for humans [21] [22] from original 150–250 Hz range primarily for rodents.

As control events for SWR⁺ candidates, SWR⁻ candidates were defined by shuffling the timestamps of SWR⁺ candidates across all trials and subjects. The defined SWR⁺/SWR⁻ candidates were visually inspected as shown in Figure 1.

2.4. Defining SWRs from putative hippocampal CA1 regions

SWRs were defined from SWR candidates in putative CA1 regions. First, putative CA1 regions were defined as follows. SWR⁺/SWR⁻ candidates in the hippocampus were embedded into a two-dimensional space based on their superimposed spike counts per unit using UMAP (uniform manifold approximation and projection) [41] in a supervised fashion (Figure 4A). The silhouette score [42], a validation barometer for clustering, was calculated from clustered samples (Table 2). The hippocampal regions with silhouette scores greater than 0.6 on average across sessions 75th percentile) (Figure 4B) were defined as putative CA1 regions, identifying five electrode positions from five patients (Table 3).

SWR⁺/SWR⁻ candidates in putative CA1 regions were defined as SWR⁺/SWR⁻, which are no longer candidates. The duration and ripple band peak amplitude of SWRs followed log-normal distributions (Figure 4C & E). SWR⁺/SWR⁻ were visually inspected as shown in Figure 1. Each of SWR periods was divided into the following periods based on the time from SWR center: pre- (at -800 to -300 ms from SWR center), mid- (at -250 to +250 ms), and post-SWR (at +300 to +800 ms).

2.5. Statistical evaluation

The Brunner–Munzel test and the Kruskal–Wallis test were executed using the *scipy* package in Python [43]. A correlational analysis was undertaken through the determination of the rank of the observed correlation coefficient in the associated set-size-shuffled surrogate, using a custom Python script. Additionally, the bootstrap test was carried out by utilizing an internally developed Python script.

3. Results

3.1. iEEG recording and neural trajectory in MTL regions during a Sternberg task

We employed a publicly available dataset [36] for this analysis. This dataset includes LFP signals (Figure 1A) within MTL regions (Table 11) during a modified Sternberg task. SWR⁺ candidates were detected from LFP signals passed through the ripple band (80–140 Hz) (Figure 1B) within all hippocampal regions (refer to Methods), while SWR⁻ candidates were defined at identical timestamps of SWR⁺ candidates but with shuffled across different trials (Figure 1). The multiunit spikes (Figure 1C) are included in the dataset as well, being established using a spike sorting algorithm [38]. Using the 50-ms binned multiunit activity without overlaps, we employed GPFA [37] to determine the neural trajectory (or factors) of the MTL regions by session and region (Figure 1D). Each factor was z-normalized by session and region (for example, session #2 in AHL of subject #1). The Euclidean distance from the origin (*O*) was calculated (Figure 1E).

3.2. Hippocampal neural trajectory correlated with a Sternberg task

In Figure 2A, the median neural trajectories of 50 trials were depicted as point clouds within the three major factor space. The optimal embedding dimension for the GPFA model was determined to be three using the elbow method (Figure 2B). The trajectory distance from the origin (*O*) ($\|g_F\|$, $\|g_E\|$, $\|g_M\|$, and $\|g_R\|$) of the hippocampus was larger than those of the EC and amygdala (Figure C & D).¹

Similarly, the distance among geometric medians of the four phases were calculated: $\|g_F g_E\|$, $\|g_F g_M\|$, $\|g_F g_R\|$, $\|g_E g_M\|$, $\|g_E g_R\|$, and $\|g_M g_R\|$. Again, the hippocampus showed larger distances among phases compared to both the EC and amygdala.²

¹Hippocampus: Distance = 1.11 [1.01], median [IQR], $n = 195,681$ timepoints; EC: Distance = 0.94 [1.10], median [IQR], $n = 133,761$ timepoints; Amygdala: Distance = 0.78 [0.88], median [IQR], $n = 165,281$ timepoints.

²Hippocampus: Distance = 0.60 [0.70], median [IQR], $n = 8,772$ combinations; EC: Distance = 0.28 [0.52], median [IQR], $n = 5,017$ combinations ($p < 0.01$; Brunner–Munzel test); Amygdala: Distance = 0.24 [0.42], median [IQR], $n = 7,466$ combinations ($p < 0.01$; Brunner–Munzel test).

3.3. Memory load-dependent neural trajectory distance between the encoding and retrieval states in the hippocampus

Regarding the memory load of the Stenberg task, correct rate of trials and set size (= the number of alphabetical letters to encode) were negatively correlated (Figure 3A).³ Similarly, response time and set size were positively correlated (Figure 3B).⁴

Furthermore, similarly, set size and the trajectory distance between the encoding and retrieval phases ($\log_{10}||g_{EGR}||$) were positively correlated (Figure 3C).⁵, while distances between other phase combinations did not yield no significant correlations (Figures 3D & S2).

3.4. Detection of hippocampal SWR from putative CA1 regions

Under the aim to improve the precision of recording sites and the detection of SWRs, we estimated electrodes in CA1 regions of the hippocampus based on observing distinct multiunit spike patterns during SWR events. For each session and hippocampal region, SWR⁺/SWR⁻ candidates were embedded into a two-dimensional space via UMAP (Figure 4A).⁶ We calculated the silhouette score as a measure of clustering quality (Figure 4B & Table 2). Recording sites with an average silhouette score across sessions exceeding 0.6 were defined as putative CA1 regions⁷ (Tables 2 & 3). Five putative CA1 regions were identified, and the four of them had not been labeled as seizure onset zones (Table 1).

³Correct rate: set size four (0.99 ± 0.11 , mean \pm SD; $n = 333$ trials) vs. set size six (0.93 ± 0.26 ; $n = 278$ trials; $p < 0.001$, Brunner–Munzel test with Bonferroni correction) and set size eight (0.87 ± 0.34 ; $n = 275$ trials; $p < 0.05$; Brunner–Munzel test with Bonferroni correction). Overall, $p < 0.001$ for Kruskal–Wallis test; correlation coefficient = -0.20, $p < 0.001$.

⁴Response time: set size four (1.26 ± 0.45 s; $n = 333$ trials) vs. set size six (1.53 ± 0.91 s; $n = 278$ trials) and set size eight (1.66 ± 0.80 s; $n = 275$ trials). All comparisons $p < 0.001$, Brunner–Munzel test with Bonferroni correction; $p < 0.001$ for Kruskal–Wallis test; correlation coefficient = 0.22, $p < 0.001$.

⁵Correlation between set size and $\log_{10}||g_{EGR}||$: correlation coefficient = 0.05, $p < 0.001$. Specific values: $||g_{EGR}|| = 0.54$ [0.70] for set size four trials, $n = 447$; $||g_{EGR}|| = 0.58$ [0.66] for set size six trials, $n = 381$; $||g_{EGR}|| = 0.61$ [0.63] for set size eight trials, $n = 395$.

⁶For illustrative purposes, consider the AHL in session #1 of subject #1.

⁷The identified regions were: AHL of subject #1, AHR of subject #3, PHL of subject #4, AHL of subject #6, and AHR of subject #9.

Subsequently, SWR⁺/SWR⁻ candidates within these putative CA1 regions were labeled SWR⁺ and SWR⁻, respectively⁸ (Table 3). Both SWR⁺ and SWR⁻ exhibited an identical duration⁹ (Figure 4C) due to their definitions, following a log-distribution profile. A increase in SWR⁺ incidence was detected during the initial 400 ms of the retrieval phase¹⁰ (Figure 4D). Additionally, the peak ripple band amplitude of SWR⁺ exceeded that of SWR⁻ and followed a log-normal distribution (Figure 4E).¹¹

3.5. Transient neural trajectory change in the hippocampus during SWR

The distances of trajectory from the origin (*O*) during SWR events in both the encoding and retrieval phases were calculated (Figure 5A). Given the distance increase during SWR as shown in Figure 5A, we categorized each SWR into three stages: pre-, mid-, and post-SWR. Subsequently, the distances from *O* during these SWR periods are represented as $||pre-eSWR^+||$, $||mid-eSWR^+||$, and so on.

$||mid-eSWR^+||$ ¹² was larger than $||pre-eSWR^+||$ ¹³, and $||mid-rSWR^+||$ ¹⁴ was larger than $||pre-rSWR^+||$ in both Match IN and Mismatch OUT tasks.¹⁵

3.6. Visualization of hippocampal neural trajectory during SWR in two-dimensional spaces

Based on our observations of neural trajectory ‘jump’ during SWR (Figure 5), we visualized the three-dimensional trajectories of pre-, mid-, and post-SWR events during the encoding and retrieval phases (Figure

⁸Definitions lead to equal counts for both categories: SWR⁺ ($n = 1,170$) and SWR⁻ ($n = 1,170$).

⁹Definitions lead to equal duration for both categories: SWR⁺ (93.0 [65.4] ms) and SWR⁻ (93.0 [65.4] ms).

¹⁰SWR⁺ increased against the bootstrap sample; 95th percentile = 0.42 [Hz]; $p < 0.05$.

¹¹SWR⁺ (3.05 [0.85] SD of baseline, median [IQR]; $n = 1,170$) vs. SWR⁻ (2.37 [0.33] SD of baseline, median [IQR]; $n = 1,170$; $p < 0.001$; Brunner–Munzel test).

¹²1.25 [1.30], median [IQR], $n = 1,281$, in Match IN task; 1.12 [1.35], median [IQR], $n = 1,163$, in Mismatch OUT task

¹³1.08 [1.07], median [IQR], $n = 1,149$, in Match IN task; 0.90 [1.12], median [IQR], $n = 1,088$, in Mismatch OUT task

¹⁴1.32 [1.24], median [IQR], $n = 935$, in Match IN task; 1.15 [1.26], median [IQR], $n = 891$, in Mismatch OUT task

¹⁵1.19 [0.96], median [IQR], $n = 673$, in Match IN task; 0.94 [0.88], median [IQR], $n = 664$, in Mismatch OUT task

6), the distance between which was memory-load dependent (Figure 3).

To achieve the visualization in two dimension spaces, peri-SWR trajectories were linearly aligned by positioning \mathbf{g}_E at the origin (0, 0) and \mathbf{g}_R at ($\|\mathbf{g}_{EGR}\|$, 0). These aligned trajectories were rotated around the \mathbf{g}_{EGR} axis (= x-axis). Thus, distances from the origin O and angles between \mathbf{g}_{EGR} in the original three-dimensional spaces are preserved in these two-dimensional ones.

The scatter plot in these two-dimensional spaces illustrates characteristic distributions of peri-SWR trajectories based on phases and task types. For instance, it is observable that $\|\text{mid-eSWR}^+\|$ is larger than $\|\text{pre-eSWR}^+\|$ (Figure 6B), consistent with our earlier findings (Figure 5).

3.7. Fluctuations of hippocampal neural trajectories between encoding and retrieval states

Subsequently, we checked trajectory *directions* based on $\overrightarrow{\mathbf{g}_{EGR}}$. SWR directions were defined by neural trajectory at -250 ms and $+250$ ms from their center (*i.e.*, $\overrightarrow{\text{eSWR}^+}$).

The density of $\overrightarrow{\text{eSWR}^+} \cdot \overrightarrow{\mathbf{g}_{EGR}}$, $\overrightarrow{\text{rSWR}^-} \cdot \overrightarrow{\mathbf{g}_{EGR}}$, and $\overrightarrow{\text{eSWR}^-} \cdot \overrightarrow{\mathbf{g}_{EGR}}$ were calculated (Figure 7A–D). $\overrightarrow{\text{rSWR}^-} \cdot \overrightarrow{\mathbf{g}_{EGR}}$ showed biphasic distributions.

By taking the differences between the distribution of $\overrightarrow{\text{rSWR}^+} \cdot \overrightarrow{\mathbf{g}_{EGR}}$ (Figure 7A & B) and those of $\overrightarrow{\text{rSWR}^-} \cdot \overrightarrow{\mathbf{g}_{EGR}}$ (Figure 7C & D), the contributions of SWR were calculated (Figure 7E & F), revealing a shift in the direction of $\overrightarrow{\mathbf{g}_{EGR}}$ (Figure 7E & F; *red rectangles*).

Additionally, only in Mismatch OUT task, $\overrightarrow{\text{eSWR}^+} \cdot \overrightarrow{\mathbf{g}_{EGR}}$ was less than $\overrightarrow{\text{eSWR}^-} \cdot \overrightarrow{\mathbf{g}_{EGR}}$ (baseline periods) (Figure 7F; *pink circles*); in other words, eSWR and rSWR directed in the adverse direction solely in Mismatch OUT task but in Match IN task (Figure 7E; *pink circles*).

4. Discussion

This study hypothesized that hippocampal neurons exhibit distinct representations, or trajectories, in low-dimensional spaces during a WM task in humans, particularly during SWR periods. First, we projected the multiunit spikes in MTL regions during a Sternberg task onto three-dimensional spaces by GPFA (Figure 1D–E and Figure 2A). The distance of trajectory among WM

phases ($\|\mathbf{g}_{FGE}\|$, $\|\mathbf{g}_{FGM}\|$, $\|\mathbf{g}_{FGR}\|$, $\|\mathbf{g}_{EGM}\|$, $\|\mathbf{g}_{EGR}\|$, and $\|\mathbf{g}_{MGR}\|$) was larger in the hippocampus than the EC and amygdala (Figure 2E), showing more dynamical neural activity in the hippocampus during the WM task. Additionally, the distance of trajectory between the encoding and retrieval phases in the hippocampus ($\|\mathbf{g}_{FGE}\|$) was positively correlated with memory load (Figure 3C–D), indicating it as a reflection of WM processing. Furthermore, the neural trajectory in the hippocampus showed transient increase during SWRs (Figure 5). Finally, the hippocampal neural trajectory fluctuated between encoding and retrieval states, with a shift from encoding to retrieval during SWR events (Figure 7). In sum, these results demonstrated the hippocampal neural behavior in a WM task in humans.

First, we found that the distance of the neural trajectory among the four phases ($\|\mathbf{g}_{FGE}\|$, $\|\mathbf{g}_{FGM}\|$, $\|\mathbf{g}_{FGR}\|$, $\|\mathbf{g}_{EGM}\|$, $\|\mathbf{g}_{EGR}\|$, and $\|\mathbf{g}_{MGR}\|$) was longer in the hippocampus compared to the EC and amygdala, even considering the distance from O ($\|\mathbf{g}_F\|$, $\|\mathbf{g}_E\|$, $\|\mathbf{g}_M\|$, and $\|\mathbf{g}_R\|$) in those regions (Figure 2C–E). These results indicate hippocampal participation in the WM task, which is partially supported by previous findings of hippocampal persistent firing in the maintenance phase [3] [4] [5] [6]. However, by applying GPFA to multiunit activity during the 1-s level resolution of WM task, we revealed that the neural trajectory in low dimensional space displayed memory-load dependency between the encoding and retrieval phase, represented as $\|\mathbf{g}_{EGR}\|$ (Figure 3). Overall, these results provide evidence that the hippocampus is linked to WM processing.

The validity of our analysis of confining to putative CA1 regions (Figure 4) is supported by several factors. First, this targeted approach stems from well-established observations that SWRs are time-locked to synchronous spike bursts of interneurons and pyramidal neurons [44] [45] [46] [47], potentially around 50 μm radius of the recording site [48]. Additionally, in the present study, we found the increase in SWRs' incidence at 0–400 ms of the retrieval phase (Figure 4D). This result is consistent with previous reports showing increased SWR occurrence before spontaneous verbal recall [21] [22]. Thus, our result is not only consistent but also extends the finding to a triggered retrieval condition. Moreover, the log-normal distributions of SWR duration and ripple band peak amplitude observed in this study (Figure 4C & E) align with the consensus

in this field [39]. Therefore, our approach of limiting recording sites for putative CA1 regions would have contributed to precision of SWR detection. One limitation is that the increase in trajectory distance from *O* during SWR (Figure 5) would have been biased to greater due to the channel selection; however, this is not critical for our major findings.

Interestingly, the trajectory directions in the retrieval phase oscillated between the encoding and retrieval states both in baseline and SWR periods (Figure 7C & D). In addition, the balance of such fluctuation was shifted from the encoding to retrieval state during SWR (Figure 7E & F). These results are again consistent with previous reports suggesting SWR's role in memory recall [21] [22]. Our result adds another layer of understanding, that is, SWR occurs when hippocampal representation proceeds "from encoding" to retrieval states. Therefore, our results provide new aspects of hippocampal representations: (i) neural fluctuations between encoding and retrieval states during a WM task and (ii) SWR as a switching representation from encoding to retrieval states.

Moreover, our study reveals WM-task type specific directions between encoding- and retrieval-SWRs (Figure 7E–F). Specifically, eSWR and rSWR directed in the adverse direction not in Match IN but in Mismatch OUT task. These result might be explained by the memory engram theory [49]. In fact, Match In task exposed subjects to once-seen letter, while Mismatch OUT task a novel letter which was not included in the encoding phase. These results suggest that SWR is related to working cognitive processess in humans.

In conclusion, our study has demonstrated that hippocampal activity fluctuates between encoding and retrieval states during a WM task and exhibits a significant transition "from encoding" to retrieval during SWR periods.

References

- [1] W. B. Scoville, B. Milner, LOSS OF RECENT MEMORY AFTER BILATERAL HIPPOCAMPAL LESIONS, *Journal of Neurology, Neurosurgery, and Psychiatry* 20 (1) (1957) 11–21. URL <https://www.ncbi.nlm.nih.gov/pmc/articles/PMC497229/>
- [2] L. R. Squire, The Legacy of Patient H.M. for Neuroscience, *Neuron* 61 (1) (2009) 6–9. doi:10.1016/j.neuron.2008.12.023. URL <https://www.ncbi.nlm.nih.gov/pmc/articles/PMC2649674/>
- [3] E. Boran, T. Fedele, P. Klaver, P. Hilfiker, L. Stieglitz, T. Grunwald, J. Sarnthein, Persistent hippocampal neural firing and hippocampal-cortical coupling predict verbal working memory load, *Science Advances* 5 (3) (2019) eaav3687. doi:10.1126/sciadv.aav3687. URL <https://www.science.org/doi/10.1126/sciadv.aav3687>
- [4] J. Kamiński, S. Sullivan, J. M. Chung, I. B. Ross, A. N. Mamelak, U. Rutishauser, Persistently active neurons in human medial frontal and medial temporal lobe support working memory, *Nature Neuroscience* 20 (4) (2017) 590–601, number: 4 Publisher: Nature Publishing Group. doi:10.1038/nn.4509. URL <https://www.nature.com/articles/nn.4509>
- [5] S. Kornblith, R. Q. Quiroga, C. Koch, I. Fried, F. Mormann, Persistent Single-Neuron Activity during Working Memory in the Human Medial Temporal Lobe, *Current Biology* 27 (7) (2017) 1026–1032, publisher: Elsevier. doi:10.1016/j.cub.2017.02.013. URL [https://www.cell.com/current-biology/abstract/S0960-9822\(17\)30149-5](https://www.cell.com/current-biology/abstract/S0960-9822(17)30149-5)
- [6] M. C. M. Faraut, A. A. Carlson, S. Sullivan, O. Tudusciuc, I. Ross, C. M. Reed, J. M. Chung, A. N. Mamelak, U. Rutishauser, Dataset of human medial temporal lobe single neuron activity during declarative memory encoding and recognition, *Scientific Data* 5 (1) (2018) 180010, number: 1 Publisher: Nature Publishing Group. doi:10.1038/sdata.2018.10. URL <https://www.nature.com/articles/sdata201810>
- [7] A. A. Borders, C. Ranganath, A. P. Yonelinas, The hippocampus supports high-precision binding in visual working memory, *Hippocampus* 32 (3) (2022) 217–230. doi:10.1002/hipo.23401.
- [8] J. Li, D. Cao, S. Yu, X. Xiao, L. Imbach, L. Stieglitz, J. Sarnthein, T. Jiang, Functional specialization and interaction in the amygdala-hippocampus circuit during working memory processing, *Nature Communications* 14 (1) (2023) 2921, number: 1 Publisher: Nature Publishing Group. doi:10.1038/s41467-023-38571-w. URL <https://www.nature.com/articles/s41467-023-38571-w>
- [9] V. Dimakopoulos, P. Mégevand, L. H. Stieglitz, L. Imbach, J. Sarnthein, Information flows from hippocampus to auditory cortex during replay of verbal working memory items, *eLife* 11 (2022) e78677, publisher: eLife Sciences Publications, Ltd. doi:10.7554/eLife.78677. URL <https://doi.org/10.7554/eLife.78677>
- [10] G. Buzsáki, Hippocampal sharp wave-ripple: A cognitive biomarker for episodic memory and planning, *Hippocampus* 25 (10) (2015) 1073–1188, _eprint: <https://onlinelibrary.wiley.com/doi/pdf/10.1002/hipo.22488>. doi:https://doi.org/10.1002/hipo.22488. URL <https://onlinelibrary.wiley.com/doi/abs/10.1002/hipo.22488>
- [11] M. A. Wilson, B. L. McNaughton, Reactivation of hippocampal ensemble memories during sleep, *Science (New York, N.Y.)* 265 (5172) (1994) 676–679. doi:10.1126/science.8036517.

- [12] Z. Nádasdy, H. Hirase, A. Czurkó, J. Csicsvari, G. Buzsáki, Replay and Time Compression of Recurring Spike Sequences in the Hippocampus, *Journal of Neuroscience* 19 (21) (1999) 9497–9507, publisher: Society for Neuroscience Section: ARTICLE. doi:10.1523/JNEUROSCI.19-21-09497.1999. URL <https://www.jneurosci.org/content/19/21/9497>
- [13] A. K. Lee, M. A. Wilson, Memory of sequential experience in the hippocampus during slow wave sleep, *Neuron* 36 (6) (2002) 1183–1194. doi:10.1016/s0896-6273(02)01096-6.
- [14] K. Diba, G. Buzsáki, Forward and reverse hippocampal place-cell sequences during ripples, *Nature Neuroscience* 10 (10) (2007) 1241–1242, number: 10 Publisher: Nature Publishing Group. doi:10.1038/nn1961. URL <https://www.nature.com/articles/nn1961>
- [15] T. J. Davidson, F. Kloosterman, M. A. Wilson, Hippocampal replay of extended experience, *Neuron* 63 (4) (2009) 497–507. doi:10.1016/j.neuron.2009.07.027.
- [16] G. Girardeau, K. Benchenane, S. I. Wiener, G. Buzsáki, M. B. Zugaro, Selective suppression of hippocampal ripples impairs spatial memory, *Nature Neuroscience* 12 (10) (2009) 1222–1223. doi:10.1038/nn.2384. URL <http://www.nature.com/articles/nn.2384>
- [17] V. Ego-Stengel, M. A. Wilson, Disruption of ripple-associated hippocampal activity during rest impairs spatial learning in the rat, *Hippocampus* 20 (1) (2010) 1–10. doi:10.1002/hipo.20707.
- [18] A. Fernández-Ruiz, A. Oliva, E. Fermino de Oliveira, F. Rocha-Almeida, D. Tingley, G. Buzsáki, Long-duration hippocampal sharp wave ripples improve memory, *Science* (New York, N.Y.) 364 (6445) (2019) 1082–1086. doi:10.1126/science.aax0758. URL <https://www.ncbi.nlm.nih.gov/pmc/articles/PMC6693581/>
- [19] J. Kim, A. Joshi, L. Frank, K. Ganguly, Cortical-hippocampal coupling during manifold exploration in motor cortex, *Nature* (2022) 1–8 Publisher: Nature Publishing Group. doi:10.1038/s41586-022-05533-z. URL <https://www.nature.com/articles/s41586-022-05533-z>
- [20] C.-T. Wu, D. Haggerty, C. Kemere, D. Ji, Hippocampal awake replay in fear memory retrieval, *Nature Neuroscience* 20 (4) (2017) 571–580. doi:10.1038/nn.4507.
- [21] Y. Norman, E. M. Yeagle, S. Khuvis, M. Harel, A. D. Mehta, R. Malach, Hippocampal sharp-wave ripples linked to visual episodic recollection in humans, *Science* 365 (6454) (2019) eaax1030. doi:10.1126/science.aax1030. URL <https://www.sciencemag.org/lookup/doi/10.1126/science.aax1030>
- [22] Y. Norman, O. Raccach, S. Liu, J. Parvizi, R. Malach, Hippocampal ripples and their coordinated dialogue with the default mode network during recent and remote recollection, *Neuron* 109 (17) (2021) 2767–2780.e5, publisher: Elsevier. doi:10.1016/j.neuron.2021.06.020. URL [https://www.cell.com/neuron/abstract/S0896-6273\(21\)00461-X](https://www.cell.com/neuron/abstract/S0896-6273(21)00461-X)
- [23] C. J. Behrens, L. P. van den Boom, L. de Hoz, A. Friedman, U. Heinemann, Induction of sharp wave-ripple complexes in vitro and reorganization of hippocampal networks, *Nature Neuroscience* 8 (11) (2005) 1560–1567, number: 11 Publisher: Nature Publishing Group. doi:10.1038/nn1571. URL <https://www.nature.com/articles/nn1571>
- [24] H. Norimoto, K. Makino, M. Gao, Y. Shikano, K. Okamoto, T. Ishikawa, T. Sasaki, H. Hioki, S. Fujisawa, Y. Ikegaya, Hippocampal ripples down-regulate synapses, *Science* (New York, N.Y.) 359 (6383) (2018) 1524–1527. doi:10.1126/science.aao0702.
- [25] S. P. Jadhav, C. Kemere, P. W. German, L. M. Frank, Awake Hippocampal Sharp-Wave Ripples Support Spatial Memory, *Science* 336 (6087) (2012) 1454–1458, publisher: American Association for the Advancement of Science. doi:10.1126/science.1217230. URL <https://www.science.org/doi/abs/10.1126/science.1217230>
- [26] J. O’Keefe, J. Dostrovsky, The hippocampus as a spatial map: Preliminary evidence from unit activity in the freely-moving rat, *Brain Research* 34 (1971) 171–175, place: Netherlands Publisher: Elsevier Science. doi:10.1016/0006-8993(71)90358-1.
- [27] J. O’Keefe, Place units in the hippocampus of the freely moving rat, *Experimental Neurology* 51 (1) (1976) 78–109. doi:10.1016/0014-4886(76)90055-8. URL <https://www.sciencedirect.com/science/article/pii/0014488676900558>
- [28] A. D. Ekstrom, M. J. Kahana, J. B. Caplan, T. A. Fields, E. A. Isham, E. L. Newman, I. Fried, Cellular networks underlying human spatial navigation, *Nature* 425 (6954) (2003) 184–188, number: 6954 Publisher: Nature Publishing Group. doi:10.1038/nature01964. URL <https://www.nature.com/articles/nature01964>
- [29] K. B. Kjelstrup, T. Solstad, V. H. Brun, T. Hafting, S. Leutgeb, M. P. Witter, E. I. Moser, M.-B. Moser, Finite Scale of Spatial Representation in the Hippocampus, *Science* 321 (5885) (2008) 140–143, publisher: American Association for the Advancement of Science. doi:10.1126/science.1157086. URL <https://www.science.org/doi/abs/10.1126/science.1157086>
- [30] C. D. Harvey, F. Collman, D. A. Dombeck, D. W. Tank, Intracellular dynamics of hippocampal place cells during virtual navigation, *Nature* 461 (7266) (2009) 941–946, number: 7266 Publisher: Nature Publishing Group. doi:10.1038/nature08499. URL <https://www.nature.com/articles/nature08499>
- [31] H. Zhang, P. D. Rich, A. K. Lee, T. O. Sharpee, Hippocampal spatial representations exhibit a hyperbolic geometry that expands with experience, *Nature Neuroscience* (Dec. 2022). doi:10.1038/s41593-022-01212-4. URL <https://www.nature.com/articles/s41593-022-01212-4>
- [32] P. A. Naber, F. H. Lopes da Silva, M. P. Witter, Reciprocal connections between the entorhinal cortex and hippocampal fields CA1 and the subiculum are in register with the projections from CA1 to the subiculum, *Hippocampus* 11 (2) (2001) 99–104, _eprint: <https://onlinelibrary.wiley.com/doi/pdf/10.1002/hipo.1028>. doi:10.1002/hipo.1028. URL <https://onlinelibrary.wiley.com/doi/abs/10.1002/hipo.1028>

- [33] N. M. van Strien, N. L. M. Cappaert, M. P. Witter, The anatomy of memory: an interactive overview of the parahippocampal-hippocampal network, *Nature Reviews Neuroscience* 10 (4) (2009) 272–282, number: 4 Publisher: Nature Publishing Group. doi:10.1038/nrn2614.
URL <https://www.nature.com/articles/nrn2614>
- [34] B. A. Strange, M. P. Witter, E. S. Lein, E. I. Moser, Functional organization of the hippocampal longitudinal axis, *Nature Reviews Neuroscience* 15 (10) (2014) 655–669, number: 10 Publisher: Nature Publishing Group. doi:10.1038/nrn3785.
URL <https://www.nature.com/articles/nrn3785>
- [35] R. J. Gardner, E. Hermansen, M. Pachitariu, Y. Burak, N. A. Baas, B. A. Dunn, M.-B. Moser, E. I. Moser, Toroidal topology of population activity in grid cells, *Nature* 602 (7895) (2022) 123–128, number: 7895 Publisher: Nature Publishing Group. doi:10.1038/s41586-021-04268-7.
URL <https://www.nature.com/articles/s41586-021-04268-7>
- [36] E. Boran, T. Fedele, A. Steiner, P. Hilfiker, L. Stieglitz, T. Grunwald, J. Sarthain, Dataset of human medial temporal lobe neurons, scalp and intracranial EEG during a verbal working memory task, *Scientific Data* 7 (1) (2020) 30, number: 1 Publisher: Nature Publishing Group. doi:10.1038/s41597-020-0364-3.
URL <https://www.nature.com/articles/s41597-020-0364-3>
- [37] B. M. Yu, J. P. Cunningham, G. Santhanam, S. I. Ryu, K. V. Shenoy, M. Sahani, Gaussian-Process Factor Analysis for Low-Dimensional Single-Trial Analysis of Neural Population Activity, *Journal of Neurophysiology* 102 (1) (2009) 614–635. doi:10.1152/jn.90941.2008.
URL <https://www.ncbi.nlm.nih.gov/pmc/articles/PMC2712272/>
- [38] J. Niediek, J. Boström, C. E. Elger, F. Mormann, Reliable Analysis of Single-Unit Recordings from the Human Brain under Noisy Conditions: Tracking Neurons over Hours, *PLOS ONE* 11 (12) (2016) e0166598, publisher: Public Library of Science. doi:10.1371/journal.pone.0166598.
URL <https://journals.plos.org/plosone/article?id=10.1371/journal.pone.0166598>
- [39] A. A. Liu, S. Henin, S. Abbaspoor, A. Bragin, E. A. Buffalo, J. S. Farrell, D. J. Foster, L. M. Frank, T. Gedankien, J. Gotman, J. A. Guidera, K. L. Hoffman, J. Jacobs, M. J. Kahana, L. Li, Z. Liao, J. J. Lin, A. Losonczy, R. Malach, M. A. van der Meer, K. McClain, B. L. McNaughton, Y. Norman, A. Navas-Olive, L. M. de la Prida, J. W. Rueckemann, J. J. Sakon, I. Skelin, I. Soltesz, B. P. Staresina, S. A. Weiss, M. A. Wilson, K. A. Zaghloul, M. Zugaro, G. Buzsáki, A consensus statement on detection of hippocampal sharp wave ripples and differentiation from other fast oscillations, *Nature Communications* 13 (1) (2022) 6000, number: 1 Publisher: Nature Publishing Group. doi:10.1038/s41467-022-33536-x.
URL <https://www.nature.com/articles/s41467-022-33536-x>
- [40] K. Kay, M. Sosa, J. E. Chung, M. P. Karlsson, M. C. Larkin, L. M. Frank, A hippocampal network for spatial coding during immobility and sleep, *Nature* 531 (7593) (2016) 185–190. doi:10.1038/nature17144.
- [41] L. McInnes, J. Healy, N. Saul, L. Großberger, UMAP: Uniform Manifold Approximation and Projection, *Journal of Open Source Software* 3 (29) (2018) 861. doi:10.21105/joss.00861.
URL <https://joss.theoj.org/papers/10.21105/joss.00861>
- [42] P. J. Rousseeuw, Silhouettes: A graphical aid to the interpretation and validation of cluster analysis, *Journal of Computational and Applied Mathematics* 20 (1987) 53–65. doi:10.1016/0377-0427(87)90125-7.
URL <https://www.sciencedirect.com/science/article/pii/0377042787901257>
- [43] P. Virtanen, R. Gommers, T. E. Oliphant, M. Haberland, T. Reddy, D. Cournapeau, E. Burovski, P. Peterson, W. Weckesser, J. Bright, S. J. van der Walt, M. Brett, J. Wilson, K. J. Millman, N. Mayorov, A. R. J. Nelson, E. Jones, R. Kern, E. Larson, C. J. Carey, Polat, Y. Feng, E. W. Moore, J. VanderPlas, D. Laxalde, J. Perktold, R. Cimrman, I. Henriksen, E. A. Quintero, C. R. Harris, A. M. Archibald, A. H. Ribeiro, F. Pedregosa, P. van Mulbregt, SciPy 1.0 Contributors, SciPy 1.0: fundamental algorithms for scientific computing in Python, *Nature Methods* 17 (2020) 261–272, aDS Bibcode: 2020NatMe..17..261V. doi:10.1038/s41592-019-0686-2.
URL <https://ui.adsabs.harvard.edu/abs/2020NatMe..17..261V>
- [44] G. Buzsáki, Two-stage model of memory trace formation: a role for "noisy" brain states, *Neuroscience* 31 (3) (1989) 551–570. doi:10.1016/0306-4522(89)90423-5.
- [45] M. L. V. Quyen, A. Bragin, R. Staba, B. Crépon, C. L. Wilson, J. Engel, Cell Type-Specific Firing during Ripple Oscillations in the Hippocampal Formation of Humans, *Journal of Neuroscience* 28 (24) (2008) 6104–6110, publisher: Society for Neuroscience Section: Brief Communications. doi:10.1523/JNEUROSCI.0437-08.2008.
URL <https://www.jneurosci.org/content/28/24/6104>
- [46] S. Royer, B. V. Zemelman, A. Losonczy, J. Kim, F. Chance, J. C. Magee, G. Buzsáki, Control of timing, rate and bursts of hippocampal place cells by dendritic and somatic inhibition, *Nature Neuroscience* 15 (5) (2012) 769–775, number: 5 Publisher: Nature Publishing Group. doi:10.1038/nn.3077.
URL <https://www.nature.com/articles/nn.3077>
- [47] N. Hájos, M. R. Karlócai, B. Németh, I. Ulbert, H. Monyer, G. Szabó, F. Erdélyi, T. F. Freund, A. I. Gulyás, Input-output features of anatomically identified CA3 neurons during hippocampal sharp wave/ripple oscillation in vitro, *The Journal of Neuroscience: The Official Journal of the Society for Neuroscience* 33 (28) (2013) 11677–11691. doi:10.1523/JNEUROSCI.5729-12.2013.
- [48] E. W. Schomburg, C. A. Anastassiou, G. Buzsáki, C. Koch, The Spiking Component of Oscillatory Extracellular Potentials in the Rat Hippocampus, *The Journal of Neuroscience* 32 (34) (2012) 11798–11811. doi:10.1523/JNEUROSCI.0656-12.2012.
URL <https://www.ncbi.nlm.nih.gov/pmc/articles/PMC3459239/>
- [49] X. Liu, S. Ramirez, P. T. Pang, C. B. Puryear, A. Govindarajan, K. Deisseroth, S. Tonegawa, Optogenetic stimulation of a hippocampal engram activates fear memory recall, *Nature* 484 (7394) (2012) 381–385, number: 7394 Publisher: Nature

Contributors

Y.W. and T.Y. conceptualized the study; Y.W. performed the data analysis; Y.W. and T.Y. wrote the original draft; and all authors reviewed the final manuscript.

Acknowledgments

This research was funded by a grant from the Exploratory Research for Advanced Technology (JPM-JER1801).

Declaration of Interests

The authors declare that they have no competing interests.

Data and code availability

The data is available on G-Node (<https://doi.gin.g-node.org/10.12751/g-node.d76994/>). The source code is available on GitHub (<https://github.com/yanagisawa-lab/hippocampal-neural-fluctuation-during-a-WM-task-in-humans>).

Inclusion and Diversity Statement

We support inclusive, diverse, and equitable conduct of research.

Declaration of Generative AI in Scientific Writing

The authors employed ChatGPT, provided by OpenAI, for enhancing the manuscript's English language quality. After incorporating the suggested improvements, the authors meticulously revised the content. Ultimate responsibility for the final content of this publication rests entirely with the authors.

Tables

Subject ID	of sessions	AHL	AHR	PHL	PHR	ECL	ECR	AL	AR	SOZ
1	4	o	x	o	o	o	x	o	x	"AHR, LR"
2	7	o	o	o	o	o	o	o	o	"AHR, PHR"
3	3	o	o	o	o	o	o	o	x	"AHL, PHL"
4	2	o	o	o	o	o	o	o	o	"AHL, AHR, PHL, PHR"
5	3	o	x	x	o	x	x	o	x	DRR
6	6	o	o	o	o	o	o	o	o	"AHL, PHL, ECL, AL"
7	4	o	o	o	o	o	o	o	o	"AHR, PHR"
8	5	o	o	o	o	o	o	o	o	ECR
9	2	o	o	o	o	o	o	o	o	"ECR, AR"

Table 1 – Electrode positions of the dataset

The electrode positions and the seizure onset zones. Regions marked as "o" were available, but those marked as "x" (*navy*) were not available in the dataset. Abbreviations: AHL, left hippocampal head; AHR, right hippocampal head; PHL, left hippocampal body; PHR, right hippocampal body; ECL, left entorhinal cortex; ECR, right entorhinal cortex; AL, left amygdala; AR, right amygdala, SOZ: seizure onset zone.

Subject	AHL	AHR	PHL	PHR
1	0.60 ± 0.14	n.a.	n.a.	0.1 ± 0
2	0.21 ± 0.16	0.17 ± 0.21	0.18 ± 0.22	0.20 ± 0.15
3	0.40 ± 0.42	0.83 ± 0.12	n.a.	n.a.
4	0.10 ± 0.00	0.10 ± 0.00	0.90 ± 0.00	0.10 ± 0.14
5	n.a.	n.a.	n.a.	n.a.
6	0.63 ± 0.06	n.a.	n.a.	0.27 ± 0.06
7	0.10 ± 0.00	0.35 ± 0.35	0.37 ± 0.47	0.10 ± 0.00
8	0.13 ± 0.10	n.a.	0.28 ± 0.49	n.a.
9	n.a.	0.85 ± 0.07	0.15 ± 0.07	n.a.

Table 2 – The silhouette score of UMAP clustering between SWR^+ candidates and SWR^- candidates

The silhouette scores (mean ± SD for sessions by subject) of UMAP clustering on SWR^+ candidates and SWR^- candidates (Figure 4A) were based on their underlying multiunit spike patterns (mean values were 0.205 [0.285], median [IQR]; Figure 4B).

Subject ID	of sessions	of trials	ROI	of SWRs	SWR incidence [Hz]
1	2	100	AHL	274	0.34
3	2	97	AHR	325	0.42
4	2	99	PHL	202	0.26
6	2	100	AHL	297	0.37
9	2	97	AHR	72	0.09
Total = 10	Total = 493	"Total = 1,170"	0.30 ± 0.13 (mean ± SD)		

Table 3 – The number of defined SWR events

The table summarizes the statistics of putative CA1 regions and SWRs. Only the first two sessions (sessions 1 and 2) from each subject were utilized to reduce the sampling bias.

Figures

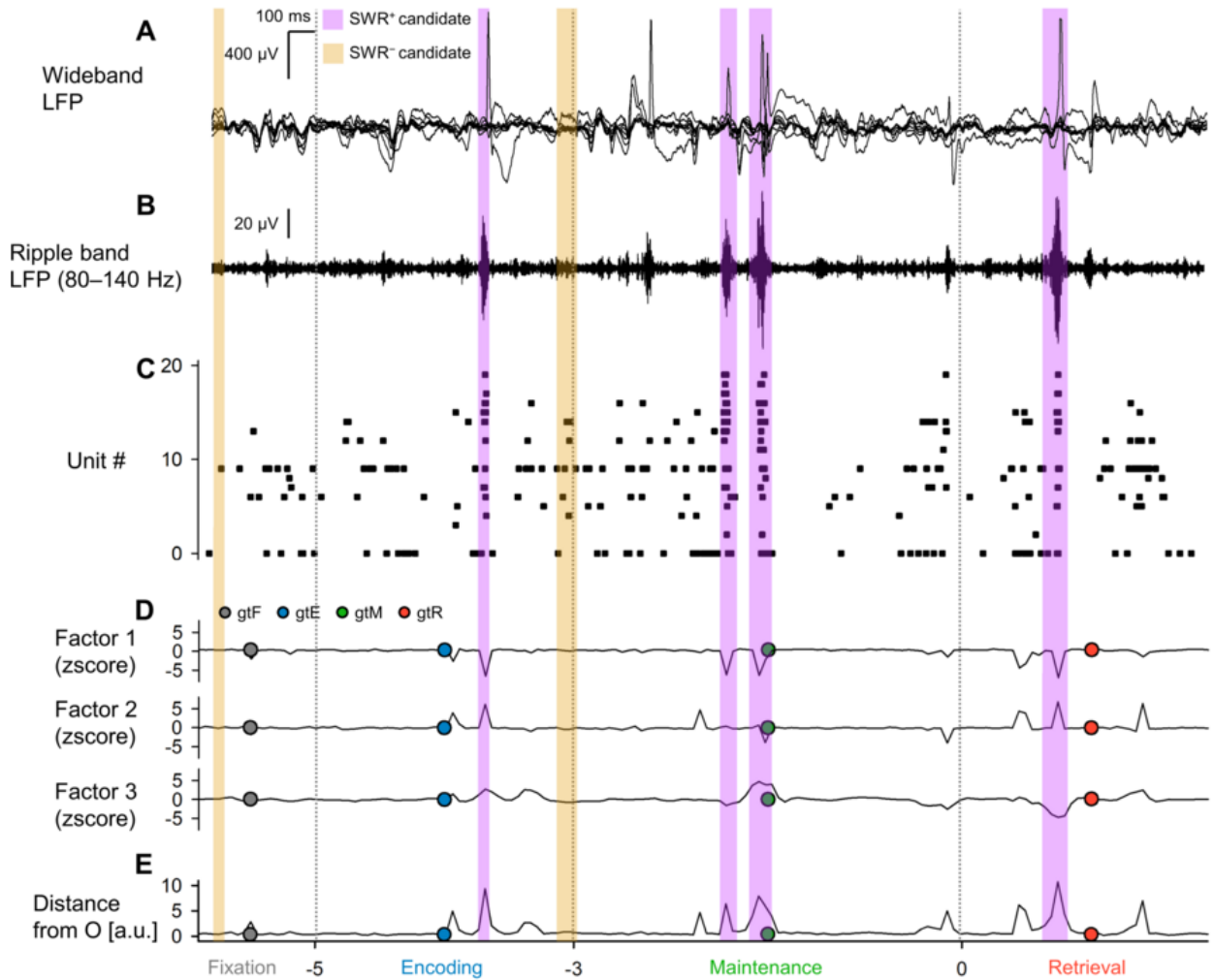


Figure 1 – Local field potential (LFP), multiunit activity, and neural trajectory of the hippocampus during a modified Sternberg task

A. Representative wideband LFP traces iEEG signals recorded in the left hippocampal head. The subject conducted a modified Sternberg working memory task, including fixation (1 s, gray), encoding (2 s, blue), maintenance (3 s, green), and retrieval (2 s, red). **B.** The corresponding ripple band LFP traces. **C.** The raster plot of multiunit spikes estimated from the LFP traces using a spike sorting algorithm [38]. **D.** Neural trajectory calculated by GPFA on spike counts per unit with 50-ms bins. The dot circles show the coordinate of geometric median for each phase. **E.** Trajectory distance from the origin *O*. Note that purple and yellow rectangles shows the timings for SWR⁺ candidates and SWR[−] candidates (control for SWR⁺), respectively.

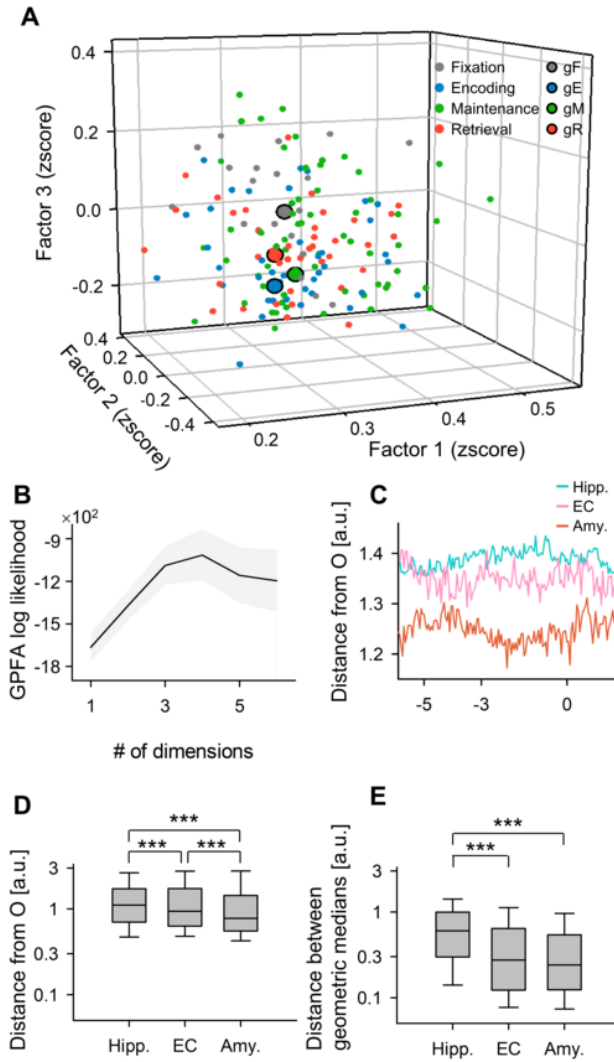


Figure 2 – State-dependent hippocampal neural trajectory

A. Neural trajectory in the first three-dimensional factors calculated by GPFA. Smaller dots indicate coordinates of 50-ms neural trajectory bins. Larger dots with *black* edges represent geometric medians for the following phases in the Sternberg working memory task: fixation (*gray*), encoding (*blue*), maintenance (*green*), and retrieval (*red*). **B.** The log-likelihood of GPFA models in relation to the number of dimensions to embed multiunit spikes in MTL regions. Notably, the optimal dimension was identified as three using the elbow method. **C.** Distance of neural trajectory from the origin (*O*) for the hippocampus (Hipp.), entorhinal cortex (EC), and amygdala (Amy.), plotted against the time from probe onset. **D.** Trajectory distance from *O* in MTL regions, with the hippocampus showing the greatest distance, followed by the EC and the Amygdala. **E.** Inter-phase trajectory distances in the MTL regions. Abbreviations:

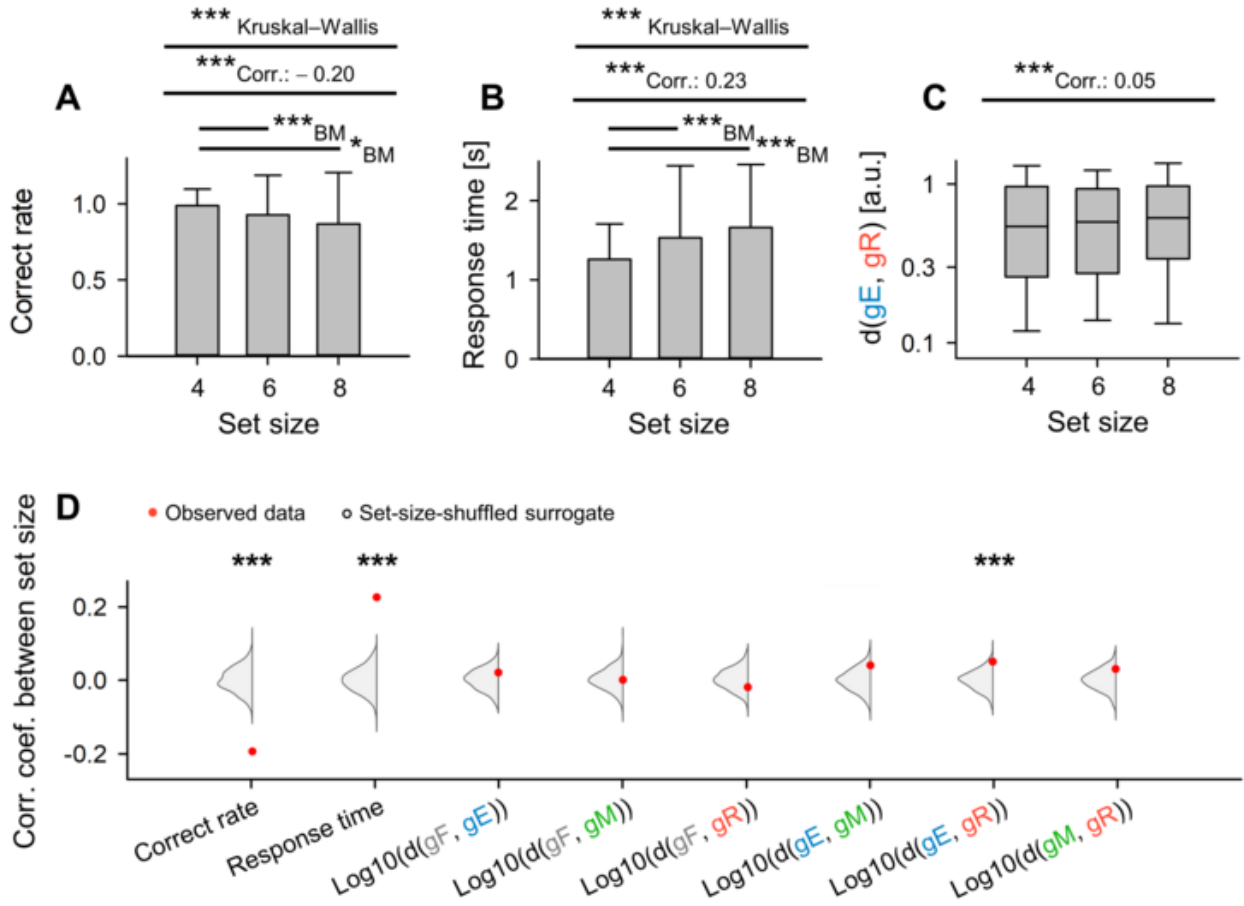


Figure 3 – Memory-load dependency in trajectory distance between encoding and retrieval states in the hippocampus

A. Set size (number of letters to encode) and correct rate in the WM task (coefficient = -0.20, *** $p < 0.001$). **B.** Set size and response time (coefficient = 0.23, *** $p < 0.001$). **C.** Set size and the inter-phase distances between encoding and retrieval phases ($\|g_E g_R\|$) (correlation coefficient = 0.05). **D.** Red dots show experimentally observed correlations between set size and the following parameters: correct rate, response time, $\log_{10} \|g_F g_E\|$, $\log_{10} \|g_F g_M\|$, $\log_{10} \|g_F g_R\|$, $\log_{10} \|g_E g_M\|$, $\log_{10} \|g_E g_R\|$, and $\log_{10} \|g_M g_R\|$. The gray kernel density plot shows corresponding set-size-shuffled surrogate ($n = 1,000$) (*** $p_s < 0.001$).

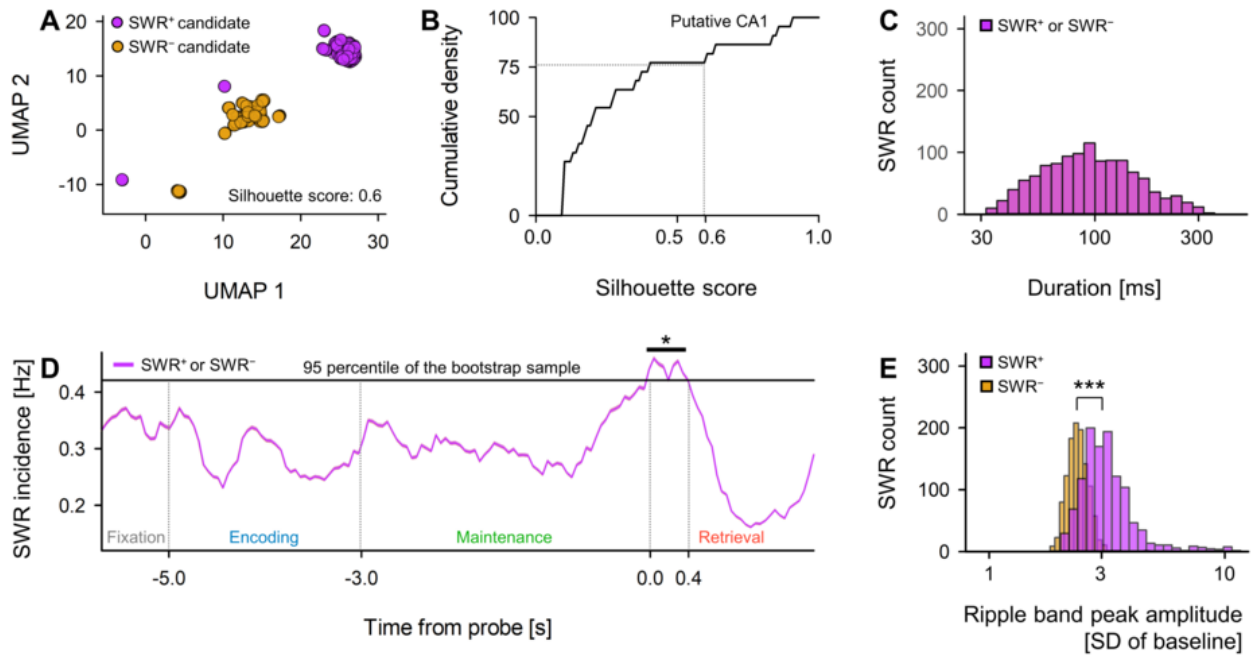


Figure 4 – SWR detection in putative CA1 regions

A. Two-dimensional UMAP (uniform manifold approximation and projection)[41] projection of multiunit spikes during SWR⁺ candidates (purple) and SWR⁻ candidates (yellow). **B.** Cumulative density plot of silhouette scores, a barometer for UMAP clustering quality, for hippocampal regions (refer to Table 2). Note that hippocampal regions with silhouette scores exceeding 0.60 (= 75th percentile) were defined as putative CA1 regions. SWR⁺ and SWR⁻ candidates recorded in these putative CA1 regions were defined as SWR⁺ and SWR⁻ ($n = 1,170$), respectively. **C.** The distributions of durations for SWR⁺ (purple) and SWR⁻ (yellow), which are identical due to their definitions (93.0 [65.4] ms, median [IQR]). **D.** SWR incidence for both SWR⁺ (purple) and SWR⁻ (yellow) relative to time from probe, represented as mean \pm 95% confidence interval, although the intervals might not be visible due to their narrow range. Note the significant elevation in SWR incidence was detected during the first 400 ms of the retrieval phase (0.421 [Hz], $*p < 0.05$, bootstrap test). **E.** The distributions of ripple band peak amplitude for SWR⁻ (yellow; 2.37 [0.33] SD of baseline, median [IQR]) and SWR⁺ (purple; 3.05 [0.85] SD of baseline, median [IQR]) ($***p < 0.001$, the Brunner–Munzel test).



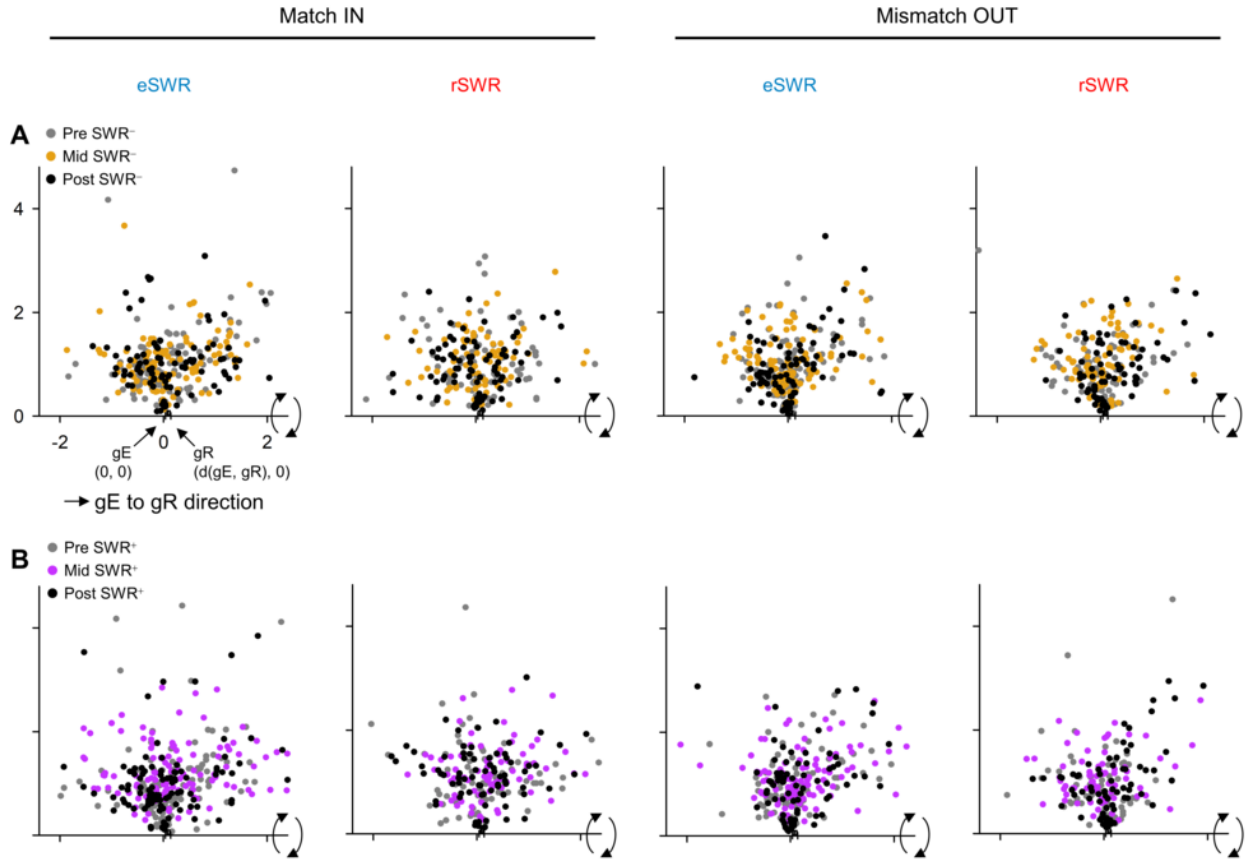


Figure 6 – Visualization of neural trajectory during SWR in two-dimensional spaces

Panels show hippocampal neural trajectories during SWR, which were projected into two-dimensional spaces. **A.** Hippocampal neural trajectories during pre- (gray), mid- (yellow), and post-SWR⁻ (black). **B.** The equivalents for SWR⁺, instead of SWR⁻. The $\|g_E g_R\|$ varied across sessions. The projection was applied as follows. First, linear transformation was applied in the way that g_E was placed at the origin $O(0, 0)$, and g_R at $(\|g_E g_R\|, 0)$. Moreover, point cloud was rotated around the $g_E g_R$ axis (= x axis) to fit in two-dimensional spaces. Thus, in these two-dimensional spaces, both the distances from O and angles between the $g_E g_R$ axis are preserved from the original three dimensional spaces. Abbreviations: SWR, sharp-wave ripple events; eSWR, SWR during the encoding phase; rSWR, SWR during the retrieval phase, SWR⁺, SWR event; SWR⁻ control events for SWR⁺; pre-SWR, mid-SWR, or post-SWR, the time interval from -800 to -250 ms, from -250 to +250 ms, or from +250 to +800 ms from the center of SWR.

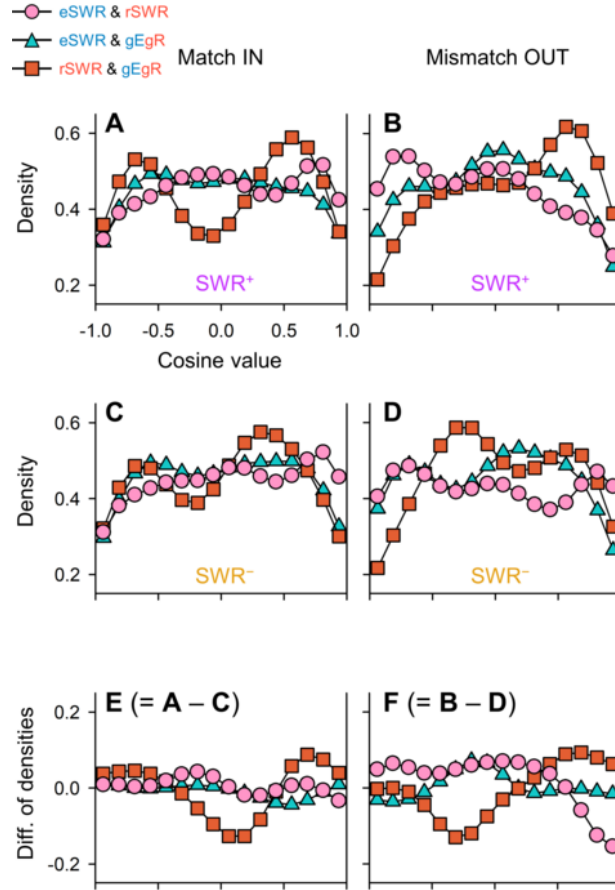


Figure 7 – Neural trajectory directions of SWR based on encoding and retrieval states

A–B Kernel density estimation (KDE) distribution of $\overrightarrow{eSWR^+} \cdot \overrightarrow{rSWR^+}$ (pink circles), $\overrightarrow{eSWR^+} \cdot \overrightarrow{gEgR}$ (blue triangles), and $\overrightarrow{rSWR^+} \cdot \overrightarrow{gEgR}$ (red rectangles) in Match In (A) and Mismatch OUT task (B). **C–D**. The corresponding distributions of SWR[−] instead of those of SWR⁺ in A–B. **E–F**. The differences in distributions of SWR⁺ and SWR[−], highlighting the SWR components ($E = C - A$; $F = B - D$). Note the biphasic distributions of $\overrightarrow{rSWR^+} \cdot \overrightarrow{gEgR}$, indicating neural fluctuation between the encoding and retrieval states during the Sternberg task. Additionally, in Mismatch OUT task, inverse directionality between $\overrightarrow{eSWR^+}$ and $\overrightarrow{rSWR^+}$ (pink circles) was found, though not in Match IN task **E–F**). Last, shifts from the retrieval to encoding states were observed for SWR components both in Match IN and Mismatch OUT tasks (red rectangles in **E–F**).